

# Flows and mixing in channels with misaligned superhydrophobic walls

Tatiana V. Nizkaya,<sup>1,\*</sup> Evgeny S. Asmolov,<sup>1,2,\*</sup> Jiajia Zhou,<sup>3,\*</sup> Friederike Schmid,<sup>3</sup> and Olga I. Vinogradova<sup>1,4,5,†</sup>

<sup>1</sup>*A.N. Frumkin Institute of Physical Chemistry and Electrochemistry,*

*Russian Academy of Science, 31 Leninsky Prospekt, 119991 Moscow, Russia*

<sup>2</sup>*Central Aero-Hydrodynamic Institute, 140180 Zhukovskiy, Moscow region, Russia*

<sup>3</sup>*Institut für Physik, Johannes Gutenberg-Universität Mainz, D55099 Mainz, Germany*

<sup>4</sup>*Department of Physics, M.V. Lomonosov Moscow State University, 119991 Moscow, Russia*

<sup>5</sup>*DWI - Leibniz Institute for Interactive Materials,*

*RWTH Aachen, Forckenbeckstr. 50, 52056 Aachen, Germany*

(Dated: March 2, 2022)

Aligned superhydrophobic surfaces with the same texture orientation reduce drag in the channel and generate secondary flows transverse to the direction of the applied pressure gradient. Here we show that a transverse shear can be easily generated by using superhydrophobic channels with misaligned textured surfaces. We propose a general theoretical approach to quantify this transverse flow by introducing the concept of an effective shear tensor. To illustrate its use, we present approximate theoretical solutions and Dissipative Particle Dynamics simulations for striped superhydrophobic channels. Our results demonstrate that the transverse shear leads to complex flow patterns, which provide a new mechanism of a passive vertical mixing at the scale of a texture period. Depending on the value of Reynolds number two different scenarios occur. At relatively low Reynolds number the flow represents a transverse shear superimposed with two co-rotating vortices. For larger Reynolds number these vortices become isolated, by suppressing fluid transport in the transverse direction.

PACS numbers: 83.50.Rp, 47.11.-j, 47.61.-k

## I. INTRODUCTION

Superhydrophobic (SH) textures have raised a considerable interest and motivated numerous studies during the past decade [1, 2]. Such surfaces in the Cassie state, i.e., where the texture is filled with gas, are extremely important in the context of fluid dynamics due to their superlubricating potential [3–5]. The use of highly anisotropic SH textures provides additional possibilities for flow manipulation. The effective hydrodynamic slip of such surfaces,  $\mathbf{b}_{\text{eff}}$ , is generally tensorial [6–9] due to secondary flows transverse to the direction of the applied pressure gradient [10, 11]. This can be used to separate particles [12] and enhance mixing rate [13] in typical for microfluidic devices low-Reynolds-numbers flows. Over the last decade, the quantitative understanding of liquid flow in SH channels with anisotropic walls was significantly expanded. However, many fundamental issues still remains challenging.

According to the modern concept of effective slip,  $\mathbf{b}_{\text{eff}}$  is a global characteristic of a channel [5], which can be applied for arbitrary channel thickness [9]. This implies that the eigenvalues depend not only on the parameters of the heterogeneous surfaces (such as local slip lengths, fractions of phases, and the texture period  $L$ ), but also on the channel thickness  $H$ . However, for a thick (compared to  $L$ ) channel they become a characteristics of a heterogeneous interface solely [3, 7, 14].

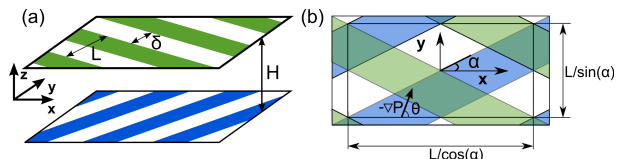


FIG. 1: (a) Cartoon showing the two identical misaligned superhydrophobic walls decorated with no-slip (white) and partial-slip (colored) stripes. (b) Top view of a periodic rectangular unit cell.

Most of the prior work has focused on the optimization of the (forward) effective slip and calculations of the eigenvalues of the effective slip-length tensor for a single 1D interface [15–19] and channels with aligned walls [8, 20] or one hydrophilic (no-slip) wall [8, 9]. The eigenvalues of  $\mathbf{b}_{\text{eff}}$  correspond to the directions of fastest and lowest effective slip. In these directions, a pressure gradient does not produce transverse flows. In other directions, however, a flow may become misaligned with the force, and transverse hydrodynamic flow can be generated. This phenomenon was also discussed only for a single interface [5, 7], for channels with symmetrically aligned stripes [10, 20] or with one no-slip wall [10, 21].

In the present paper, we show that any misalignment of textured and anisotropic walls necessarily leads to a generation of shear flow in the transverse direction, which has not been appreciated in previous work [7]. The transverse shear, in turn, generates complex flow structures at

\*These three authors contributed equally to the work.

†Corresponding author: oivinograd@yahoo.com

the scale of the texture period. We show that at low, but finite, Reynolds numbers (Re) of the channel, a transverse shear is superimposed with two co-rotating vortices. At larger Re, these vortices become isolated, by suppressing a transverse shear. Such flow structures lead to a global vertical mixing of fluids, which does not rely on the presence of confining side walls.

## II. MODEL

We consider the pressure-driven flow between two parallel stationary (passive) SH walls separated by the distance  $H$  and decorated with identical anisotropic textures of a period  $L$ , and width of the gas area  $\delta$ , so that the fraction of the slipping area is  $\phi = \delta/L$ . The lower and the upper wall textures are misaligned by an angle  $0 \leq 2\alpha \leq \pi/2$ . The flow is periodic with a rectangular unit cell as depicted in Fig. 1. We place the origin of the  $(x, y, z)$  coordinate system at the center of the cell, in the midplane, with the  $z$  axis perpendicular to the walls.

We assume the gas interface to be flat with no meniscus curvature. Such an idealized situation, which neglects an additional mechanism for a dissipation due to a meniscus, has been considered in most previous publications [11, 18, 22]. It has been shown theoretically [18, 24] that a low curvature of the meniscus expected for relatively dense textures cannot reduce the effective slippage in the Stokes regime (but note that there are still some remaining controversies in the experimental data [23, 25]). The quantitative understanding of whether and how such curvature effects could modify effective slip lengths in the case of finite Re is still challenging. This subject, which remains largely unexplored, is beyond the scope of the present work and deserves a separate study.

We finally impose no-slip at the solid area, i.e. neglect slippage of liquid [26–28] and gas [29] past hydrophobic surface, which is justified provided the nanometric slip is small compared to parameters of the texture. Prior work often assumed idealized shear-free boundary conditions over the gas sectors [22, 30, 31], so that the viscous dissipation in the underlying gas phase has been neglected. Here we will use the partial slip boundary conditions, which are the consequences of the ‘gas cushion model’ [32, 33].

## III. THEORY OF TRANSVERSE SHEAR

To address effective (‘macroscopic’) properties of the channel we evaluate the mean velocity profile of the Stokes flow ( $\text{Re} \ll 1$ ), averaged over the periodic cell in  $x, y$ . Due to the linearity of the Stokes equations, it is sufficient to consider only the flow in eigendirections of the texture. Let us first consider a pressure-driven flow with  $-\nabla P$  aligned with the  $x$ -axis ( $\theta = 0$ ). If  $-\nabla P$  is aligned with the  $y$ -axis, the flow can then be obtained by simply replacing  $\alpha$  by  $\pi/2 - \alpha$ . The symmetry of

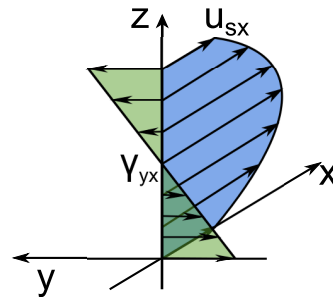


FIG. 2: Sketch of an mean velocity profile  $\langle u \rangle(z)$  given by Eq. (1). A uniform  $-\nabla P$  is applied in the  $x$ -direction.

the problem implies that the  $x$ -component of the mean velocity is symmetric in  $z$  and its  $y$ -component is anti-symmetric. For the Stokes flow the mean velocity profile is scaled by  $U_0 = -H^2 \nabla P / (2\mu)$  and has the following form:

$$\langle \mathbf{u} \rangle(z) = \left( \frac{1}{4} - z^2 \right) \mathbf{e}_x + u_{sx} \mathbf{e}_x + \gamma_{yx} z \mathbf{e}_y, \quad (1)$$

where coordinates are scaled by  $H$ ,  $u_{sx}$  is the slip velocity in the  $x$ -direction and  $\gamma_{yx}$  is the transverse shear rate. Therefore, the first term represents the conventional Poiseuille flow, the second term is a slip-driven (forward) plug flow, and the last term is a linear shear flow in the transverse direction. The laminar flow in the channel is a linear superposition of these three terms as shown in Fig. 2. Eq.(1) can therefore be seen as a generalization of an earlier idea, formulated for a thick channel [7], to an arbitrary channel situation.

To quantify the effective properties of the channel, we now introduce the flow and shear rates averaged over the cell volume  $V$ :

$$\mathbf{Q} = \frac{1}{V} \int \mathbf{u}_\tau dV = -\frac{H^2}{12\mu} \mathbf{k} \cdot \nabla P, \quad (2)$$

$$\mathbf{G} = \frac{1}{V} \int \frac{\partial \mathbf{u}_\tau}{\partial z} dV = -\frac{H}{2\mu} \boldsymbol{\gamma} \cdot \nabla P, \quad (3)$$

where  $\mathbf{u}_\tau = (u_x, u_y)$  is the tangential velocity. The effective (dimensionless) effective permeability,  $\mathbf{k}$ , and shear,  $\boldsymbol{\gamma}$ , tensors can then be found by solving a local problem in the channel.

Let us note that Eq. (1) and the symmetry conditions imply that the  $\mathbf{k}$  and  $\boldsymbol{\gamma}$  tensors are:

$$\mathbf{k} = \begin{pmatrix} k_{xx}(\alpha) & 0 \\ 0 & k_{yy}(\alpha) \end{pmatrix}, \quad (4)$$

where  $k_{xx} = 1 + 6u_{sx}$  and

$$\boldsymbol{\gamma} = \begin{pmatrix} 0 & \gamma_{xy}(\alpha) \\ \gamma_{yx}(\alpha) & 0 \end{pmatrix}. \quad (5)$$

Thus, our coordinate system diagonalizes the permeability tensor. Also, due to the symmetry of the periodic cell,  $k_{yy}(\alpha) = k_{xx}(\pi/2 - \alpha)$  and  $\gamma_{xy}(\alpha) = \gamma_{yx}(\pi/2 - \alpha)$ .

To calculate  $u_{sx}(\alpha)$  and  $\gamma_{yx}(\alpha)$  we have to solve the Stokes equations on the periodic cell with spatially varying local slip lengths. The flow can be treated as a superposition of two solutions for a configuration with one SH and one hydrophilic wall, which is justified provided the thickness of the channel is large enough (see Appendix A). This simplification allows us to obtain explicit formulae for the mean slip and the shear tensor:

$$u_{sx}(\alpha) = \frac{\beta_+ + \beta_- \cos(2\alpha) + 2(\beta_+^2 - \beta_-^2)}{1 + 2\beta_+ - 2\beta_- \cos(2\alpha)}, \quad (6)$$

$$\gamma_{yx}(\alpha) = -\frac{2\beta_- \sin(2\alpha)}{1 + 2\beta_+ - 2\beta_- \cos(2\alpha)}, \quad (7)$$

where  $\beta_+ = (b_{\text{eff}}^{\parallel} + b_{\text{eff}}^{\perp})/(2H)$ ,  $\beta_- = (b_{\text{eff}}^{\parallel} - b_{\text{eff}}^{\perp})/(2H)$ . The effective slip tensor  $\mathbf{b}_{\text{eff}}$  here corresponds to a configuration with one SH wall.

The misalignment of the upper and the lower textures leads to a ‘macroscopic’ anisotropy of the flow, i.e. the effective permeability depends on the direction of the pressure gradient, and a secondary transverse flow is generated. To study this effect, we now apply  $-\nabla P$  at an angle  $0 \leq \theta \leq \pi/2$  to the  $x$ -axis. For the forward and transverse flow rate we then obtain, using the tensorial formalism [7]:

$$\begin{aligned} Q_{\text{F}}/Q_0 &= k_{xx} \cos^2 \theta + k_{yy} \sin^2 \theta, \\ Q_{\text{T}}/Q_0 &= (k_{xx} - k_{yy}) \cos \theta \sin \theta, \end{aligned} \quad (8)$$

where  $Q_0 = \frac{|\nabla P|H^2}{12\mu}$  corresponds to the Poiseuille flow in a channel with hydrophilic walls. Note that  $Q_{\text{T}}$  vanishes when  $\theta = 0$  or when stripes are crossed at a right angle,  $2\alpha = \pi/2$ . These special configurations, therefore, are equivalent to channels with impermeable side walls.

Similarly, for the mean shear rates we get

$$\begin{aligned} G_{\text{F}}/G_0 &= -(\gamma_{xy} + \gamma_{yx}) \sin \theta \cos \theta, \\ G_{\text{T}}/G_0 &= \gamma_{yx} \cos^2 \theta - \gamma_{xy} \sin^2 \theta, \end{aligned} \quad (9)$$

where  $G_0 = \frac{U_0}{H} = \frac{|\nabla P|H}{2\mu}$  is a characteristic shear rate for a hydrophilic channel. It follows from Eq. (9) that the forward shear rate,  $G_{\text{F}}$ , vanishes when  $\theta = 0$  or when  $\gamma_{xy} = -\gamma_{yx}$ , but the transverse shear rate,  $G_{\text{T}}$ , becomes zero only at  $\theta = \pm(\arctan(\gamma_{xy}/\gamma_{yx}))^{1/2}$ . However, this does not imply that the shear tensor can be diagonalized by a proper rotation of the coordinate system, since the two directions are not orthogonal in the general case.

To illustrate this general approach we focus below on specific case of SH surfaces consisting of periodic stripes, where the piecewise constant local slip lengths of (identical) textured walls vary in only one direction. In this case the  $\mathbf{k}$  and  $\boldsymbol{\gamma}$  tensors have been found using the numerical solutions of the Stokes equations [21] (see Appendix A for details), and the eigenvalues of the slip-length tensor correspond to those calculated before [9].

#### IV. SIMULATIONS AND DATA ANALYSIS

In order to assess the validity of the above theoretical approach at the relatively low Re regime and to explore what happens when Re is larger, we employ the Dissipative Particle Dynamics (DPD) simulations [34, 35] carried out using the open source package ESPResSo [36]. Specifically, we use DPD as a Navier-Stokes solver based on a fluid of non-interacting particles [16] and combine that with a tunable-slip method [37] that allows one to vary the local slip length [16, 20, 38].

Note that for misaligned stripes the simulation box depends on  $2\alpha$  due to the periodic boundary conditions in the  $x$ - and  $y$ -directions (see Fig. 1). The three dimensions of the simulation box are  $(L/\sin \alpha, L/\cos \alpha, H + 2\sigma)$ , where  $\sigma$  sets the length scale. The extra  $2\sigma$  in  $z$ -direction accounts for the depletion due to the excluded volume interaction of the impermeable surfaces. In the present study, we have used  $L = 20\sigma$ , and  $H/L = 1$  or  $0.5$ . All simulations have been performed for textures with the fraction of gas phase  $\phi = 0.5$ , where the Cassie state is typically stable. The local slip length on the slippery area was chosen to be  $b/L = 10$ , which is close to the maximum attainable local slip length at the gas area,  $b/L \simeq 16\phi$  [33], in the case of deep textures, where again the Cassie state is very stable.

With a fluid density  $\rho = 3.75\sigma^{-3}$ , a typical system consists of  $0.6\text{--}1.2 \times 10^5$  particles. The simulation starts with randomly distributed particles. The pressure-driven flow is modeled by applying to all particles an external force in the  $x$ -direction. The system is allowed to reach a steady state after  $10^6$  time steps; then the measurement is performed by averaging over  $10^5$  time steps to obtain sufficient statistics. We use a body force ranging from  $f = 0.004\varepsilon/\sigma$  to  $0.04\varepsilon/\sigma$ , where  $\varepsilon$  sets the energy scale. These values of  $f$  provide flows with Reynolds numbers varying from  $\text{Re} = 2.8$  to  $\text{Re} = 28$ . All simulations were performed with a time step  $\Delta t = 0.01\sqrt{m\varepsilon}/\sigma$ , where  $m$  is the mass of DPD particles, and the temperature of the system was set at  $\varepsilon = k_B T$ . The DPD interaction parameter is chosen at  $\gamma_{\text{DPD}} = 5.0\sqrt{m\varepsilon}/\sigma$  and the cutoff is  $1.0\sigma$ . The shear viscosity is measured to be  $\mu_s = 1.35 \pm 0.01\sqrt{m\varepsilon}/\sigma^2$ .

Mean fluxes and shear rates are calculated by averaging the simulation data over the periodic cell. The fluid velocity field obtained in simulations is used to compute a family of streamlines from the beginning to the end of the cell. These streamlines are then used to construct the vector field of fluid displacements over one texture period. Finally, to visualize the fluid mixing we define a dense uniform grid in the channel cross-section at a distance of  $N$  periods from the inlet, and for each point of this grid we then calculate backward streamlines to determine its initial position.

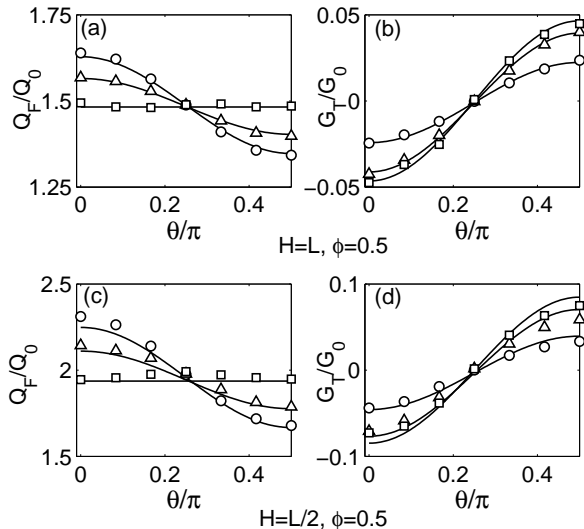


FIG. 3: Forward flow rate (a, c) and transverse shear rate (b, d) as a function of  $\theta$  computed with  $b/L = 10$ . The thickness of the channel,  $H$ , is equal to  $L$  (a, b) or  $L/2$  (c, d). Symbols show simulation results for  $Re = 2.8$  and misalignment angles  $2\alpha = \pi/6$  (circles),  $\pi/3$  (triangles), and  $\pi/2$  (squares). Solid curves are theoretical predictions for  $Re \ll 1$  (Eqs. (8) and (9)).

## V. RESULTS AND DISCUSSION

In order to assess the validity of the above theoretical approach developed for low  $Re$  we first run a set of simulations at  $Re=2.8$  in channels with different misalignment angles  $2\alpha$ , and  $H/L = 1$  and  $0.5$ . The simulation results are shown in Fig. 3. Also included are the forward fluxes and transverse shear rates calculated using Eqs. (8-9). A general conclusion is that the theoretical predictions are in excellent agreement with simulation results for  $H/L = 1$  (Fig. 3(a,b)). Even for thinner channels,  $H/L = 0.5$  (Fig. 3(c,d)), where the theory slightly underestimates the permeability and overestimates the transverse shear, which is likely due to simplifications made (see Section III and Appendix A), the agreement is quite good. Fig. 3 shows that the flow rates  $Q_F$  become maximal for  $-\nabla P$  aligned with the  $x$ -axis ( $\theta = 0$ ) and minimal if it is aligned with the  $y$ -axis ( $\theta = \pi/2$ ). These directions correspond to the largest amplitude of a transverse shear  $|G_T|$  at a given  $2\alpha$ . When the lower and upper stripes are orthogonal ( $2\alpha = \pi/2$ ),  $Q_F$  becomes independent on  $\theta$ , and we recall that in this case  $Q_T = 0$  as discussed above. This orthogonal configuration allows one to reach (at  $\theta = 0$  and  $\pi/2$ ) the largest possible amplitude of  $|G_T|$  that can be attained in the channel. Therefore, the detailed investigation of flow and mixing properties below will be restricted to this optimal configuration with  $2\alpha = \pi/2$ ,  $\theta = 0$ , and to a thinner channel,  $H/L = 0.5$ .

Now we note that our simulations, performed at small,

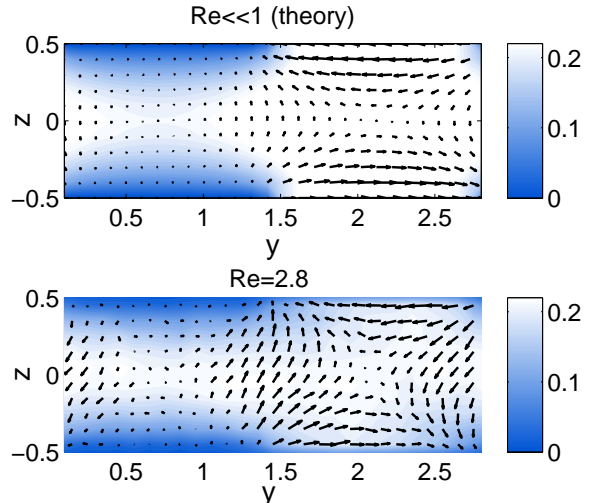


FIG. 4: Cross-sections (at  $x = 0$ ) of the velocity field ( $u_y, u_z$ ) obtained in the theory ( $Re \ll 1$ ) and simulations ( $Re = 2.8$ ). Color map shows the forward velocity  $u_x$ .

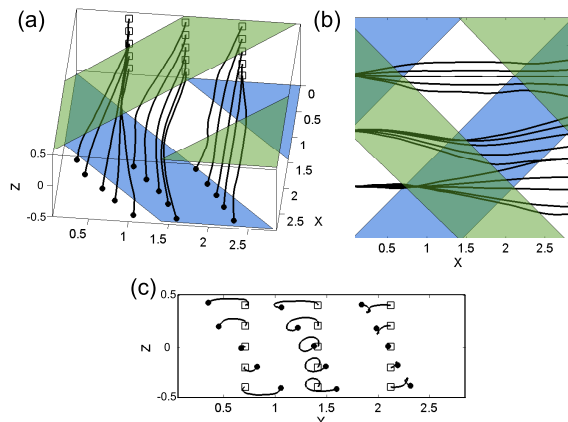


FIG. 5: 3D (a), top (b) and front (c) view of streamlines for the simulated velocity field ( $Re = 2.8$ ). Squares indicate initial positions of fluid particles, dots show their positions at the end of the periodic cell.

but finite  $Re$ , suggest that the texture misalignment leads to a complex shape of the flow on the scale of the period of the texture. In Fig. 4 we have plotted typical theoretical ( $Re \ll 1$ ) and simulation ( $Re = 2.8$ ) cross-sections of the fluid velocity. A general conclusion from this plot is that the fluid in the upper part of the channel is driven in the  $y$ -direction, but in the lower part it flows in the opposite direction, which is in agreement with our theoretical predictions of a transverse shear. A striking result emerging from this plot is that the simulated velocity field shows in addition a significant  $z$ -component at the midplane of the channel, which is likely due to a finite inertia of the fluid.

To understand the global properties of the simulated

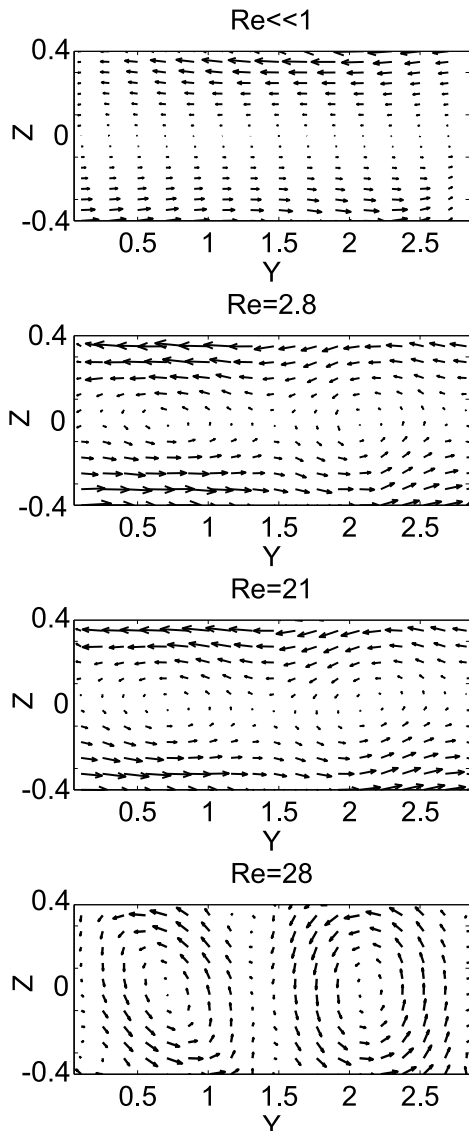


FIG. 6: Vector field of fluid displacements over one cell period in  $yz$ -plane. The velocity fields are obtained from simplified theory for  $Re \ll 1$  and simulations for  $Re = 2.8, 21$  and  $28$ .

flow, we now focus on its streamlines shown in Fig. 5. We conclude, that indeed, as expected, fluid particles are displaced in  $y$ -direction due to a generation of a non-zero mean shear. However, in addition some small (but non-zero) vertical displacement is observed, so that they reach different positions on the  $yz$ -plane after crossing a unit cell.

An explanation for an emerging flow in  $z$ -direction, not predicted by the simple Stokes theory, can be obtained if we invoke fluid inertia, which is characterized by the value of  $Re$ . To examine its significance in more details we construct a vector fields of fluid displacements over one period from the simulation data obtained at  $Re = 2.8, 21$ , and  $28$ . In Fig. 6 we plot these vector fields predicted theoretically and obtained from the sim-

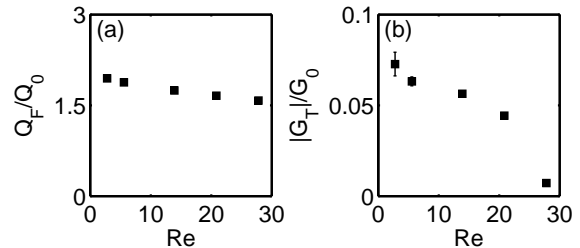


FIG. 7: Forward flow rate (a) and transverse shear rate (b) simulated at different  $Re$ .

ulations. We see that depending on the value of  $Re$ , different scenarios occur. For  $Re \ll 1$  we observe a mean shear flow with very small vertical component near the walls. At  $Re = 2.8$  and  $21$  vector fields show a different behavior, i.e. represent a uniform shear superimposed with two co-rotating vortices. Finally, at  $Re = 28$  we detect two isolated vortices and inhibited transport in  $y$ -direction.

The impact of  $Re$  on forward and transverse flows is highlighted in Fig.7. We see that the simulated  $Q_F$  remains nearly constant. In contrast, the transverse shear rate  $|G_T|$  is a relatively weakly decreasing function of  $Re$  up to  $Re \simeq 21$ , and then decreases abruptly down to a much smaller value at  $Re = 28$ .

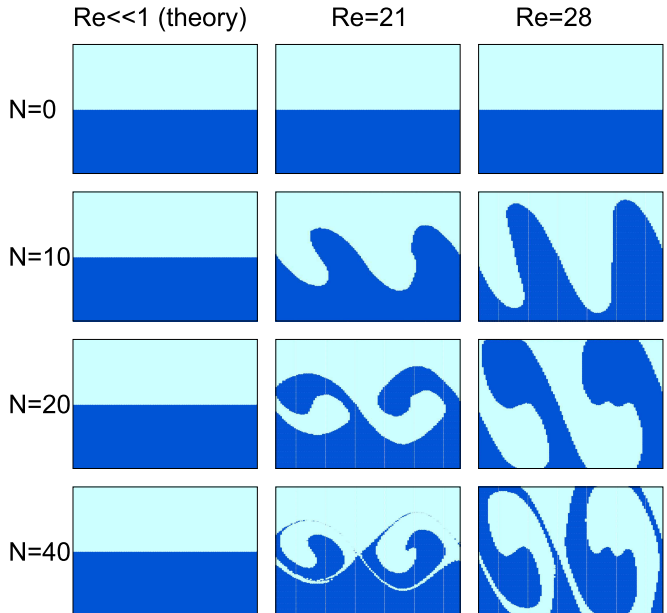


FIG. 8: Displacements of colored fluids over  $N$  periods obtained for several  $Re$ . The axis limits (not shown) are the same as in Fig. 6.

Our results have shown that flow in the channel with misaligned SH walls is much more complicated than the usual picture. The misalignment results in the generation of a transverse shear, but perhaps the most interesting

and important aspect is the interplay of this transverse flow with the finite inertia of the fluid. This leads to a vertical displacement of a fluid, which could have implication for a vertical mixing in such a channel. To understand whether these results are significant for mixing, we mark the upper and lower parts of the channel by different colors and compute the evolution of this system **over**  $N$  periods. The representative results for a contour field are shown in Fig.8. We see that no vertical mixing occurs for the Stokes flow. For  $\text{Re} = 21$  the mixing area is located in the center of the channel, but for  $\text{Re} = 28$  the whole fluid is mixed.

## VI. CONCLUSION

In this paper we have extended the tensorial description of SH channels developed earlier to configurations with misaligned textures on bottom and top walls. We prove, that effective properties of such channels are described by the permeability,  $\mathbf{k}$ , and the shear rate,  $\gamma$ , tensors, and develop a simplified theoretical approach, valid for  $\text{Re} \ll 1$ , to quantify them. We checked the validity of this approach by DPD simulations and found that theoretical predictions are in quantitative agreement with the simulation results obtained at finite, but moderate  $\text{Re}$ .

Simulations have also shown that at finite  $\text{Re}$  the flow generated by this transverse shear provides a basis for a new mixing mechanism of the fluids in microfluidic devices. Unlike most classical mixers [4, 39, 40], where vortices are created both by large-scale inhomogeneities of patterned walls and by the side walls of the channel, in our misaligned configuration the mixing occurs on the scale of the texture period. It does not depend on the presence of confining side walls and is, therefore, insensitive to the cross-sectional aspect ratio of the channel. We also recall that in microfluidic devices the mixing is normally controlled by viscous terms, so that the form of the flow is independent on  $\text{Re}$  and remains the same up to  $\text{Re} \simeq 100$  [41]. In contrast, our vertical mixing is driven by fluid inertia even at very moderate  $\text{Re}$ , and becomes more pronounced with the increase in  $\text{Re}$ .

Finally, we mention that our results can be immediately extended to a situation of a channel with a periodically changing orientation of top and bottom stripes, which could lead to a chaotic advection [42–44], currently exploited mostly in the ‘herringbone’-type mixers [39, 41].

## Acknowledgments

This research was partly supported by the Russian Foundation for Basic Research (grant 15-01-03069), the EU IRSES DCP-PhysBio (grant N269139), and by the VW foundation. The simulations were carried out using computational resources at the John von Neumann Institute for Computing (NIC Jülich), the High Perfor-

mance Computing Center Stuttgart (HLRS) and Mainz University (MOGON).

## Appendix A: Calculation of permeability and shear tensors

We write the velocity field in the cell  $\mathbf{u}(x, y, z) = (u_x, u_y, u_z)$  in the form

$$\mathbf{u} = \langle \mathbf{u} \rangle + \mathbf{u}_1 + \mathbf{u}_2. \quad (\text{A1})$$

Here  $\mathbf{u}_1, \mathbf{u}_2$  are perturbations with zero mean over the cell volume due to heterogeneous slippage at the lower and upper walls, respectively.

Since the problem is linear, we can formulate the boundary conditions for  $\mathbf{u}_1, \mathbf{u}_2$  at the lower wall as

$$\begin{aligned} z = -\frac{1}{2} : \quad \mathbf{u}_2 = \mathbf{0}, \quad u_{z1} = 0, \\ \mathbf{u}_{\tau 1} - b_1 \frac{\partial \mathbf{u}_{\tau 1}}{\partial z} = -u_{sx} \mathbf{e}_x + \frac{\gamma_{yx}}{2} \mathbf{e}_y \\ + b_1 \left( \mathbf{e}_x + \gamma_{yx} \mathbf{e}_y + \frac{\partial \mathbf{u}_{\tau 2}}{\partial z} \right), \end{aligned} \quad (\text{A2})$$

and at the upper wall as

$$\begin{aligned} z = \frac{1}{2} : \quad \mathbf{u}_1 = \mathbf{0}, \quad u_{z2} = 0, \\ \mathbf{u}_{\tau 2} - b_2 \frac{\partial \mathbf{u}_{\tau 2}}{\partial z} = -u_{sx} \mathbf{e}_x - \frac{\gamma_{yx}}{2} \mathbf{e}_y \\ + b_2 \left( -\mathbf{e}_x + \gamma_{yx} \mathbf{e}_y + \frac{\partial \mathbf{u}_{\tau 1}}{\partial z} \right), \end{aligned} \quad (\text{A3})$$

where  $b_{1,2}(x, y)$  are the local slip lengths on the lower and the upper wall, respectively.

The perturbations decay at a distance from the wall of the order of  $L$ . For this reason, in the case of a sufficiently thick channel we can expect that the disturbance gradients at the opposite walls are small:

$$\begin{aligned} z = -\frac{1}{2} : \quad \left| \frac{\partial \mathbf{u}_{\tau 1}}{\partial z} \right| \ll \left| \frac{\partial \langle \mathbf{u} \rangle}{\partial z} \right|, \\ z = \frac{1}{2} : \quad \left| \frac{\partial \mathbf{u}_{\tau 2}}{\partial z} \right| \ll \left| \frac{\partial \langle \mathbf{u} \rangle}{\partial z} \right|. \end{aligned} \quad (\text{A4})$$

Then the solution is the superposition of two flows in a channel with a SH and a no-slip walls. These flows can be calculated numerically [21]. The validity of the assumption, Eq.(A4), is verified by evaluating the disturbance gradients induced by a SH wall on a no-slip wall. The gradients are small compared to the wall gradient for the Poiseuille flow,  $|\partial \langle \mathbf{u} \rangle / \partial z| = 2$ , at  $H/L > 0.5$  (see Fig. 9).

Consider now the flow induced by the undisturbed shear rate  $\mathbf{e}_x + \gamma_{yx} \mathbf{e}_y$  at the bottom wall. Projections of the unit vectors to the  $(\xi, \eta)$  coordinate system with the axes parallel and perpendicular to the stripes (see Fig. 10) are

$$\begin{aligned} \mathbf{e}_x &= \mathbf{e}_\xi \cos \alpha - \mathbf{e}_\eta \sin \alpha, \\ \mathbf{e}_y &= \mathbf{e}_\xi \sin \alpha + \mathbf{e}_\eta \cos \alpha. \end{aligned} \quad (\text{A5})$$

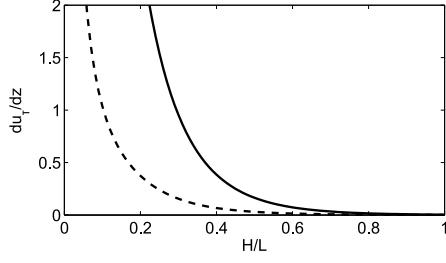


FIG. 9: Maximal values of the velocity disturbance gradient at the opposite walls for  $b/L = 10$ ,  $\phi = \delta/L = 1/2$ ,  $2\alpha = \pi/2$  against the channel thickness. Solid curve shows  $\frac{\partial u_{x1}}{\partial z}$ , dashed curve plots  $\frac{\partial u_{y1}}{\partial z}$  at  $z = 1/2$ .

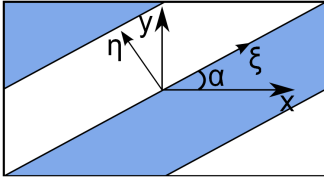


FIG. 10: Coordinate system  $(\xi, \eta)$ , associated with the lower wall, see Eq.(A5).

It follows from Eqs. (A3) and (A5) that at  $z = -1/2$  the mean slip velocity and the shear rate are

$$\begin{aligned} \langle \mathbf{u}_\tau \rangle &= \left( u_{sx} \cos \alpha - \frac{\gamma_{yx}}{2} \sin \alpha \right) \mathbf{e}_\xi \\ &\quad - \left( u_{sx} \sin \alpha + \frac{\gamma_{yx}}{2} \cos \alpha \right) \mathbf{e}_\eta, \end{aligned} \quad (\text{A6})$$

$$\left\langle \frac{\partial \mathbf{u}_\tau}{\partial z} \right\rangle = (\cos \alpha + \gamma_{yx} \sin \alpha) \mathbf{e}_\xi - (\sin \alpha - \gamma_{yx} \cos \alpha) \mathbf{e}_\eta.$$

From (A6) we have

$$\frac{b_{\text{eff}}^\parallel}{H} = \frac{u_{sx} \cos \alpha - \frac{\gamma_{yx}}{2} \sin \alpha}{\cos \alpha + \gamma_{yx} \sin \alpha}, \quad (\text{A7})$$

$$\frac{b_{\text{eff}}^\perp}{H} = \frac{u_{sx} \sin \alpha + \frac{\gamma_{yx}}{2} \cos \alpha}{\sin \alpha - \gamma_{yx} \cos \alpha}. \quad (\text{A8})$$

Here the components of the effective slip length tensor  $\mathbf{b}_{\text{eff}}$  correspond to the usual configuration with a SH and a no-slip walls [9]. Thus we obtain from (A7), (A8):

$$u_{sx}(\alpha) = \frac{\beta_+ + \beta_- \cos(2\alpha) + 2(\beta_+^2 - \beta_-^2)}{1 + 2\beta_+ - 2\beta_- \cos(2\alpha)}, \quad (\text{A9})$$

$$\gamma_{yx}(\alpha) = -\frac{2\beta_- \sin(2\alpha)}{1 + 2\beta_+ - 2\beta_- \cos(2\alpha)}, \quad (\text{A10})$$

where  $\beta_+ = (b_{\text{eff}}^\parallel + b_{\text{eff}}^\perp)/(2H)$ ,  $\beta_- = (b_{\text{eff}}^\parallel - b_{\text{eff}}^\perp)/(2H)$ .

The flow in the transverse direction can be obtained by replacing  $x$  by  $y$  and  $\alpha$  by  $\pi/2 - \alpha$ . Therefore, we readily obtain the permeability tensor:

$$\mathbf{k} = \begin{pmatrix} 1 + 6u_{sx}(\alpha) & 0 \\ 0 & 1 + 6u_{sx}(\pi/2 - \alpha) \end{pmatrix}, \quad (\text{A11})$$

and the shear tensor:

$$\boldsymbol{\gamma} = \begin{pmatrix} 0 & \gamma_{yx}(\pi/2 - \alpha) \\ \gamma_{yx}(\alpha) & 0 \end{pmatrix}. \quad (\text{A12})$$

- 
- [1] D. Quere, Rep. Prog. Phys. **68**, 2495 (2005).  
[2] T. Darmanin and F. Guittard, J. Mater. Chem. A **2**, 16319 (2014).  
[3] L. Bocquet and J. L. Barrat, Soft Matter **3**, 685 (2007).  
[4] J. P. Rothstein, Annu. Rev. Fluid Mech. **42**, 89 (2010).  
[5] O. I. Vinogradova and A. L. Dubov, Mendeleev Commun. **19**, 229 (2012).  
[6] H. A. Stone, A. D. Stroock, and A. Ajdari, Annu. Rev. Fluid Mech. **36**, 381 (2004).  
[7] M. Z. Bazant and O. I. Vinogradova, J. Fluid Mech. **613**, 125 (2008).  
[8] F. Feuillebois, M. Z. Bazant, and O. I. Vinogradova, Phys. Rev. Lett. **102**, 026001 (2009).  
[9] S. Schmieschek, A. V. Belyaev, J. Harting, and O. I. Vinogradova, Phys. Rev. E **85**, 016324 (2012).  
[10] F. Feuillebois, M. Z. Bazant, and O. I. Vinogradova, Phys. Rev. E **82**, 055301(R) (2010).  
[11] O. I. Vinogradova and A. V. Belyaev, J. Phys.: Cond. Matter **23**, 184104 (2011).  
[12] D. Pimponi, M. Chinappi, P. Gualtieri, and C. M. Casciola, Microfluidics Nanofluidics **16**, 571 (2014).  
[13] J. Ou, G. R. Moss, and J. P. Rothstein, Phys. Rev. E **76**, 016304 (2007).  
[14] K. Kamrin, M. Bazant, and H. A. Stone, J. Fluid Mech. **658**, 409 (2010).  
[15] A. V. Belyaev and O. I. Vinogradova, J. Fluid Mech. **652**, 489 (2010).  
[16] J. Zhou, E. S. Asmolov, F. Schmid, and O. I. Vinogradova, J. Chem. Phys. **139**, 174708 (2013).  
[17] N. V. Priezjev, J. Chem. Phys. **135**, 204704 (2011).  
[18] C. Ybert, C. Barentin, C. Cottin-Bizonne, P. Joseph, and L. Bocquet, Phys. Fluids **19**, 123601 (2007).  
[19] C. O. Ng, H. C. W. Chu, and C. Y. Wang, Phys. Fluids **22**, 102002 (2010).  
[20] J. Zhou, A. V. Belyaev, F. Schmid, and O. I. Vinogradova, J. Chem. Phys. **136**, 194706 (2012).  
[21] T. V. Nizkaya, E. S. Asmolov, and O. I. Vinogradova, Soft Matter **9**, 11671 (2013).  
[22] N. V. Priezjev, A. A. Darhuber, and S. M. Troian, Phys. Rev. E **71**, 041608 (2005).  
[23] J. Ou, B. Perot, and J. P. Rothstein, Phys. Fluids **16**, 4635 (2004).

- [24] A. Davis and E. Lauga, *Phys. Fluids* **21**, 011701 (2009).
- [25] G. Bolognesi, C. Cottin-Bizonne, and C. Pirat, *Phys. Fluids* **26**, 082004 (2014).
- [26] O. I. Vinogradova, *Int. J. Miner. Proc.* **56**, 31 (1999).
- [27] O. I. Vinogradova, K. Koynov, A. Best, and F. Feuillebois, *Phys. Rev. Lett.* **102**, 118302 (2009).
- [28] L. Joly, C. Ybert, and L. Bocquet, *Phys. Rev. Lett.* **96**, 046101 (2006).
- [29] D. Seo and W. A. Ducker, *Phys. Rev. Lett.* **111**, 174502 (2013).
- [30] J. R. Philip, *J. Appl. Math. Phys.* **23**, 353 (1972).
- [31] E. Lauga and H. A. Stone, *J. Fluid Mech.* **489**, 55 (2003).
- [32] O. I. Vinogradova, *Langmuir* **11**, 2213 (1995).
- [33] T. V. Nizkaya, E. S. Asmolov, and O. I. Vinogradova, *Phys. Rev. E* **90**, 043017 (2014).
- [34] P. J. Hoogerbrugge and J. M. V. A. Koelman, *Europhys. Lett.* **19**, 155 (1992).
- [35] P. Español and P. Warren, *Europhys. Lett.* **30**, 191 (1995).
- [36] H. Limbach, A. Arnold, B. Mann, and C. Holm, *Comput. Phys. Commun.* **174**, 704 (2006).
- [37] J. Smiatek, M. Allen, and F. Schmid, *Eur. Phys. J. E* **26**, 115 (2008).
- [38] E. S. Asmolov, J. Zhou, F. Schmid, and O. I. Vinogradova, *Phys. Rev. E* **88**, 023004 (2013).
- [39] A. D. Stroock, S. K. Dertinger, G. M. Whitesides, and A. Ajdari, *Anal. Chem.* **74**, 5306 (2002).
- [40] D. R. Mott, P. B. Howell Jr., J. P. Golden, C. R. Kaplan, F. S. Ligler, and E. S. Oran, *Lab on a Chip* **6**, 540 (2006).
- [41] A. D. Stroock, S. K. W. Dertinger, A. Ajdari, I. Mezić, H. A. Stone, and G. M. Whitesides, *Science* **295**, 647 (2002).
- [42] S. Wiggins and J. M. Ottino, *Phil. Trans. R. Soc. A* **362**, 937 (2004).
- [43] H. Aref, *Journal of Fluid Mechanics* **143**, 1 (1984).
- [44] M. A. Stremler, F. R. Haselton, and H. Aref, *Phil. Trans. R. Soc. Lond. A* **362**, 1019 (2004).